Investigation on cation distribution and luminescence in spinel phase γ-Ga$_{3-\delta}$O$_4$: Sm nanostructures using X-ray absorption spectroscopy†

Aditya Sharma, [ID] *[a] Mayora Varshney,[a] Hyun-Joon Shin,[b] Keun Hwa Chae[a] and Sung Ok Won*[a]

In this study, spectroscopic investigations are employed to quantify the Ga distribution over the tetrahedral/octahedral sites and to assimilate the luminescence properties in the barely reported γ-Ga$_{2.67}$O$_4$: Sm nanoparticles. O K-edge XANES are convincing the decreased electron density in the outermost hybrid orbits of O 2p and Ga 4p, and the movement of p electrons to the inner hybrid orbits with s character under the distorted oxygen environment of γ-Ga$_{2.67}$O$_4$: Sm nanoparticles. The Ga K/L-edge XANES and Sm L$_3$/M$_{5,4}$-edge XANES results have confirmed Ga^{3+} and Sm^{3+} ions, respectively, in the γ-Ga$_{2.67}$O$_4$: Sm nanoparticles. Quantitative determination of the cation distribution is performed by applying Ga К-edge XANES data analysis, which is further substantiated by an EXAFS data simulation, and conveys a Ga-O4 tetrahedra/Ga-O6 octahedra ratio (Ga(t)/Ga(o)) of ~0.9, ~1.4, ~1.5 and ~1.6 for the β-Ga$_2$O$_3$, γ-Ga$_{2.67}$O$_4$, γ-Ga$_{2.67}$O$_4$: 5Sm and γ-Ga$_{2.67}$O$_4$: 10Sm samples, respectively, which signify the Sm doping induced deformation of Ga-O6 octahedra via the formation of oxygen defects. Multiple luminescence centres, facilitated by the Ga-O6 octahedra distortion, O vacancies and Sm^{3+} ions, have helped in a significant enhancement of the emission characteristics. Our spectroscopy investigations, with the help of XANES and EXAFS, may open new opportunities to the mechanistic understanding of metal-O polyhedra alteration induced fruition of physical/chemical properties in the less explored meta stable phases of other complex oxides.

Introduction

Gallium-oxide (Ga$_2$O$_3$) polymorphs *i.e.*; α-Ga$_2$O$_3$, β-Ga$_2$O$_3$, γ-Ga$_2$O$_3$, δ-Ga$_2$O$_3$ and ε-Ga$_2$O$_3$,[1-4] have evoked much attention because of their wide range of applications in optoelectronics, gas sensing, magnetic tunnel junctions, photo-catalysis, biomedical fields, *etc.*[5-9] Among all the known phases of Ga$_2$O$_3$, γ-Ga$_2$O$_3$ is the class of material which possesses a cubic or defective-spinel crystal structure with uneven occupancy of Ga at the tetrahedral and octahedral sites.[2-4] The strong correlation between the metal atom site occupancy and its structural/optical/electronic properties make γ-Ga$_2$O$_3$ an attractive material for investigating the fundamental connections between the crystal/electronic structure and unexplored applications.

Most of the reports on γ-Ga$_2$O$_3$ have considered the cubic unit cell of this compound;[8,10-12] however, a defective spinel structure of γ-Ga$_2$O$_3$ (space group; *Fd$\bar{3}$m*) was recently identified by a neutron diffraction technique with four different site occupancies of Ga: tetrahedral (8a), octahedral (16d), tetrahedral (48f) and octahedral (16c).[3,4] Unlike the normal spinel-structure stoichiometry in γ-Ga$_2$O$_3$ (ideally, it should be Ga$_3$O$_4$), among every 18 cationic sites, two sites are vacant in order to retain charge neutrality.[3,4] Pair distribution function analysis was also employed to refine the γ-Ga$_2$O$_3$; however, the discrepancy between the average and local structure could not be resolved.[4] If such complications were not enough during the simulation of the γ-Ga$_2$O$_3$ structural details, investigations on the local structure determination would further be complicated in the cation deficient spinel phases of gallium oxides, such as γ-Ga$_{3-\delta}$O$_4$. The cation deficient γ-Ga$_{3-\delta}$O$_4$ phase is very similar to that of a hypothetical spinel Ga$_3$O$_4$ compound; however, less investigation has been made because of its poor thermal stability during its synthesis.

Theoretical studies have shown that the band structure of Ga$_2$O$_3$, near the Fermi level, is formed by the O 2p and Ga 4s states. The top of the valence band consists mainly of the O 2p states, with a width of 7 eV, and the bottom of the conduction band is formed by Ga 4s states.[13-15] Ga d orbitals do not

[a]*Advanced Analysis Centre, Korea Institute of Science and Technology, Seoul-02792, South Korea. E-mail: adityaiuac@gmail.com; sowon@kist.re.kr*

[b]*Pohang Accelerator Laboratory (POSTECH), Pohang-37673, South Korea*

contribute to the band structure near the Fermi level, because of the $3d^{10}$ electronic configuration of Ga d orbitals in Ga_2O_3, but facilitate a deep valence band along with the O 2s orbitals.[13,14] The octahedrally coordinated Ga atoms possess higher coordination with the surrounding O atoms, compared with the tetrahedrally coordinated Ga atoms, and, thus, the degree of covalency is higher for the tetrahedrally coordinated Ga atoms in the Ga_2O_3 lattice.[13–15] The band structure and, hence, the electronic/optical properties of Ga_2O_3 are not only sensitive to the doping of foreign element at Ga lattice sites[16,17] but may also be detonated by the distortion of the Ga–O environment or alteration in the Ga site occupancy. A small change in the Ga tetrahedral/octahedral site occupancy is expected to affect the orbital hybridization of frontier Ga 4s/4p and O 2p orbitals which, obviously, can regulate the band structure of the compound and consequently electronic/optical properties.

In the previous reports, nano/micro sized β-Ga_2O_3 particles have been extensively studied for their synthesis,[9,18–23] band structure,[15] optical[18,19] and catalyst properties.[21–23] The other polymorphous phases of gallium oxide can demonstrate exceptional metal–oxygen orbital hybridization and a perceptibly diverse band structure near the Fermi level because of the miscellaneous Ga site occupancy in the Ga_2O_3 lattice; however, their synthesis, crystal structure analysis, optical properties and local atomic/electronic structure investigations are ineffectually reported. Thus, an atomistic level investigation on the unidentified or less studied polymorphous phases, such as the cation deficient γ-$Ga_{3-\delta}O_4$, is desirable to gain control over and fabricate their nanostructures for light-emitting applications. Though the synthesis of small sized nanostructures is important for catalytic[21–23] and optical properties,[10–12,18–20] the tiny nanostructures introduce complications in the structural and electronic structure investigations because of the significant surface artefacts.[10–12,18–20] The sensitivity of the powder XRD techniques becomes poor to the structural details when the particle size reaches up to a few nanometres.[24,25] Moreover, for the case of nanocrystalline Ga_2O_3 polymorphs, the diverse occupancies of Ga atoms and cation/anion deficiencies facilitate a complex local atomic structure to the compound which may not be completely elucidated by the conventional XRD technique.[2,3] Therefore, it is necessary to apply modern techniques which not only probe the crystal structure 'locally' but also provide valuable information on the lattice disorders upon defect formation, foreign element doping and alteration in the metal element occupancy. In this regard, X-ray absorption spectroscopy (XAS), with its two branches of X-ray absorption near edge structure (XANES) and extended X-ray absorption fine structure (EXAFS), becomes the important elemental characterization technique and has been known to be highly sensitive to the local electronic/atomic structure properties and effectively overcomes the issue of sensitivity to the structure and electronic structure characterization of small sized, poorly crystalline or embedded nanostructures.[26–28] In the last few years, probing the local symmetry of the diluted doped elements,[29,30] quantification of the valence state changes of host metal ions upon foreign element doping,[31–33] changes in the orbital occupancy,[34,35] and variation in the crystal field

effects[36,37] have been studied for various compounds using the XANES. On the other side, EXAFS, due to the sensitivity to the local atomic structure, has become a powerful probing tool for determining the variation in the coordination number and bond lengths of the constituent elements of the probed material.[32–40] Besides providing detailed experimental and simulated results on the Ga_2O_3 polymorphous compounds, the XANES–EXAFS analysis presented in this article addresses various aspects. Firstly, O K-edge XANES spectra were examined to specifically look into the diversity in the oxygen environment of γ-$Ga_{3-\delta}O_4$ and β polymorphous phases and to assimilate the effect of Sm insertion on the metal 4s/4p and O 2p orbital hybridization. Secondly, quantitative determination of the cation distribution is performed by using Ga K-edge XANES and EXAFS to estimate the Ga-O4 tetrahedra and Ga-O6 octahedra proportions in β-Ga_2O_3, γ-$Ga_{3-\delta}O_4$ and Sm doped γ-$Ga_{3-\delta}O_4$. To our knowledge, the Ga-O6/Ga-O4 octahedra/tetrahedra deformation under Sm incorporation and enhancement in the emission characteristics of γ-$Ga_{3-\delta}O_4$: Sm nanoparticles are barely covered in the literature. Our spectroscopy investigations may provide mechanistic insights into the modification in the orbital hybridization of Ga 4s/4p and O 2p, Ga local site occupancy, defect formation and emission properties of the metastable γ-$Ga_{3-\delta}O_4$ phase.

Experimental

Pure and Sm-doped gallium oxide nanoparticles were synthesized using a modified non-aqueous precipitation method. All the reagents used were of analytical grade without further purification. Pure gallium oxide nanoparticles were synthesized by dissolving 2g of $Ga(NO_3)_2 \cdot xH_2O$ (gallium nitrate hydrate) into 100 ml of ethanol under vigorous magnetic stirring. However, to synthesize the Sm doped gallium oxide nanoparticles, $SmCl_3 \cdot 6H_2O$ (samarium chloride hexahydrate) was mixed with the $Ga(NO_3)_2 \cdot H_2O$, in the desired molar proportion, and then dissolved in 100 ml of ethanol with magnetic stirring for an hour. Two different molar concentrations (i.e., 5 and 10 molar percentages) of Sm^{3+} ions were applied in the present experiments. After achieving clear solutions of the precursors, the pH of the solution was raised up to 11 ± 0.2 by adding hydrazine monohydrate. As soon as the hydrazine monohydrate was added to the solution, an abrupt precipitation was achieved. The precipitates were washed several times with ethanol and then dried at 80 °C in air overnight. A fraction of a pure gallium oxide sample was also annealed at 600 °C and 900 °C in air for two hours. XRD measurements were performed by using the Bruker D8 advanced diffractometer, operated at a 40 kV accelerating voltage and 40 mA tube current. The radiation produced from the Cu target was Cu Kα of wavelength 1.5418 Å. Transmission electron microscopy (TEM) measurements were performed using the FEI (Tecnai-F20G²) transmission electron microscope operated at 200 kV. The Raman spectra were collected by using the Renishaw InVia Raman Microscope with a Nd : YAG (neodymium-doped yttrium aluminium garnet) laser, which produces 532 nm wavelength photon beam. XANES spectra at the O K-edge, Sm $M_{5,4}$-edge and Ga L-edge were

collected in the total electron yield (TEY) mode at the 10D (XAS-KIST) soft X-ray beamline at the Pohang Accelerator Laboratory (PAL), South Korea. The photon energy resolution of this beamline was better than 0.6 eV (at the O K edge). The EXAFS spectra at the Ga K-edge and Sm L_3-edge were collected at the 1D XRS KIST-PAL beam line. This beam line utilizes a Si (111) double crystal monochromator and the higher harmonics were effectively removed by detuning the crystals to 70% of the maximum intensity. This beam line has three ionization chambers for collecting the data from samples, either in the transmission or fluorescence mode. Generally, the chamber, which is used for measuring the incident beam current, is filled with He. Chambers for measuring the transmission and reference spectra are filled with N_2. For energy approaching 16 keV, an Ar gas or mixture of Ar and N_2 is preferred for these chambers; however, a mixture of He and N_2 is used when the beam energy is nearly 4 keV. N_2 in the transmission and reference chamber is the best choice for measuring spectra in the energy range 5–15 keV. Energy calibrations were made for all the measurements using reference metal foils of the constituent elements in the sample. The sample was placed between the first and the second ionization chambers, while the reference foils were placed between the second and the third ionization chambers. Photoluminescence was measured by using a 325 nm He–Cd laser as the excitation source with a power density < 0.6 W m^{-2}.

Results and discussion

X-ray diffraction, TEM and Raman studies

Fig. 1(a) shows the XRD patterns of pure, 5 mol% Sm doped, and 10 mol% Sm doped gallium oxides samples. Fig. 1(b) shows the XRD results of the 600 °C and 900 °C annealed samples. It is evident from Fig. 1(a) that the XRD patterns of the pure and Sm incorporated gallium oxide samples consist of several diffraction peaks. All the diffraction peaks of the pure and Sm doped samples were fairly matched with the cation-deficient spinel structure γ-Ga$_{2.67}$O$_4$ (space group $Fd\bar{3}m$; JCPDS#15-2085, $a = b = c = 8.238$ Å, $\alpha = \beta = \gamma = 90°$). Thus, our XRD results conveying the formation of a cation deficient γ-Ga$_{2.67}$O$_4$ phase in the present study. Hereafter, pure, 5 mol% Sm doped, and 10 mol% Sm doped samples are named as γ-Ga$_{2.67}$O$_4$, γ-Ga$_{2.67}$O$_4$: 5Sm and γ-Ga$_{2.67}$O$_4$: 10Sm, respectively. In previous reports, the cubic unit cell has been extensively assigned to the γ phases of Ga$_2$O$_3$ with the expected distribution of Ga over the tetrahedral (8a) and octahedral (16c) sites.[8,10–12] Contrary to this, we have achieved cation-defective spinel γ-Ga$_{2.67}$O$_4$ compounds in which Ga^{3+} ions can additionally distribute over the tetrahedral (48f) sites along with the tetrahedral (8a) and octahedral (16c) sites.[4] Besides the expected Ga occupancy dissimilarity in the presented synthesized compounds, there is a distinct difference in the XRD patterns of the γ-Ga$_{2.67}$O$_4$ phase and the commonly reported γ-Ga$_2$O$_3$ phase. In the inset of Fig. 1(a), we provide the diffraction patterns of JCPDS#15-2085 (for the γ-Ga$_{2.67}$O$_4$ phase) and JCPDS#20-0426 (for the commonly reported γ-Ga$_2$O$_3$ phase). It is clear from the inset of Fig. 1(a) that the peak (111), appearing at ~18.7°, is distinctly present in the XRD
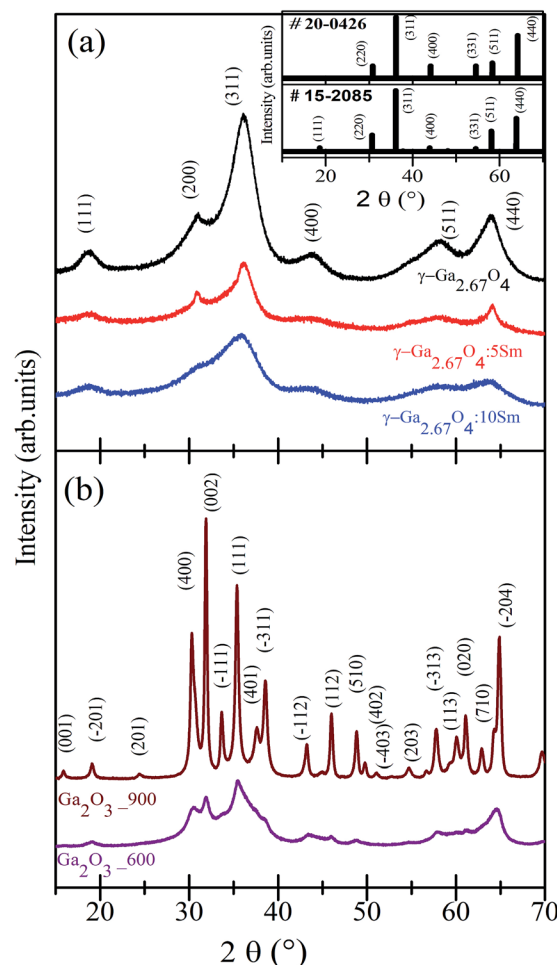

Fig. 1 (a) XRD patterns of pure and Sm doped γ-Ga$_{2.67}$O$_4$. (b) XRD patterns of the samples annealed at 600 °C and 900 °C. Spectra are vertically shifted for clarity of the data.

results of γ-Ga$_{2.67}$O$_4$ and JCPDS#15-2085, but not seen in JCPDS#20-0426 and previously reported cubic phasic γ-Ga$_2$O$_3$ nanoparticles. Synthesis of an obscured polymorphous phase of gallium oxide is intriguing and may be the consequences of non-aqueous synthesis and an implication of a highly reactive hydrazine monohydrate precursor in the present research. Hydrazine monohydrate can quickly and effectively reduce the starting reagent of Ga and form abrupt precipitation in which nuclei of gallium oxide can be formed. Such starting nuclei, if washed and filtered with ethanol (ethanol works as an effective dispersive media for the precipitates[41]), may grow into the cation deficient γ-Ga$_{2.67}$O$_4$ phase upon a low-temperature drying process (80 °C).

In previous reports, synthesis with DI water and liquid ammonia solution could only grow GaOOH kinds of phases which further transformed into α-Ga$_2$O$_3$, γ-Ga$_2$O$_3$ and β-Ga$_2$O$_3$ phases upon high-temperature annealing.[18,19] Thus, the formation of the γ-Ga$_{2.67}$O$_4$ phase in the present study, at moderate temperate, is due to the modified non-aqueous synthesis procedure with the amendment of a reactive hydrazine monohydrate precursor. No diffraction peak matched with

the other polymorphous of gallium oxide (*i.e.*, α-Ga_2O_3, β-Ga_2O_3, δ-Ga_2O_3 and ε-Ga_2O_3) or trivial phases of metallic Sm, SmO and Sm_2O_3 and, thus, the XRD results strengthen the manufacturing of single phase γ-$Ga_{2.67}O_4$: Sm in the present study. Significant XRD peak broadening and diminishing of peak intensity is seen in the Sm doped samples and could be due to a decrease of particle size and/or lattice deformation. We have calculated the crystallite size from all of the samples using the Scherrer relation; $D = 0.9\lambda/\beta \cos\theta$ (*D* is the particle size, *λ* is the wavelength of the X-rays used, *β* is the full width at half maximum of the diffraction peak, and the instrument broadening effect was not included in such calculations). Thus, the calculated sizes are 4.3 nm, 2.9 nm, 2.1 nm, 13.2 nm and 32.5 nm for the γ-$Ga_{2.67}O_4$, γ-$Ga_{2.67}O_4$: 5Sm, γ-$Ga_{2.67}O_4$: 10Sm, 600 °C annealed and 900 °C annealed samples, respectively. The XRD patterns also give an impression that there is a lower angle shifting in the diffraction peaks of the Sm doped samples, compared with pure γ-$Ga_{2.67}O_4$ (this can be easily seen in the γ-$Ga_{2.67}O_4$: 10Sm sample). Thus, $d_{(311)}$ was examined and found to be 2.488(6) Å, 2.495(2) Å and 2.519(2)Å for the γ-$Ga_{2.67}O_4$, γ-$Ga_{2.67}O_4$: 5Sm and γ-$Ga_{2.67}O_4$: 10Sm samples, respectively. The marginal increase in the $d_{(311)}$ values for Sm doped samples may arise due to the occupancy of larger Sm^{3+} ions (ionic radii ∼ 109.8 pm) at the lattice position of smaller Ga^{3+} ions (ionic radii, ∼78.0 pm). The decrease in crystallite size and increase in the $d_{(311)}$ values indicate the inhibition of crystalline growth and structural perturbation in the crystalline lattice of gallium oxide upon Sm^{3+} ion doping. Here we expect that the insertion of Sm^{3+} ions in the crystalline lattice of gallium oxide produces a strain (due to the larger ionic radii of Sm^{3+} over Ga^{3+}) which, conceivably, alters the metal–oxygen polyhedra and leads to a decline in the crystallinity of the material. Moreover, in previous reports, doping of a foreign element evidenced the non-stoichiometry of the metal–oxygen chains or segregation of the doped ions at surface/grain boundaries, which prevents the crystalline growth of the particle.[12,42] The non-stochiometric metal–oxygen grain boundaries, which can be formed by lattice-strain induced diverse metal–oxygen stacking or segregation of dopants, may increase the amorphous content in the γ-$Ga_{2.67}O_4$: Sm nanoparticles, leading to broadening of the XRD peaks and a decrease in the peak intensity. In our previous reports,[32,33] a similar trend in the XRD peak broadening and increase in the cell parameters/$d_{(hkl)}$ was observed for the Eu and Hf doped CeO_2 NPs and was ascribed to the Eu/Hf induced lattice disorders in CeO_2. Raman measurements are also convincing of the poor crystallinity in the Sm doped samples and have also ruled out a suspected phase formation (Fig. S1 and related discussion in the ESI†). The decrease in the particle size and the poor crystallinity are also seen in the TEM and FFT images of the γ-$Ga_{2.67}O_4$: 5Sm and γ-$Ga_{2.67}O_4$: 10Sm samples and tally with the findings from XRD results (Fig. S2 and related discussion in the ESI†). XRD patterns in Fig. 1(b) are certainly dissimilar with respect to the XRD patterns of γ-$Ga_{2.67}O_4$ and suggest a different phase formation in the 600 °C and 900 °C annealed samples. XRD patterns of the 600 °C and 900 °C annealed samples are fairly matched with the monoclinic unit cell of the β-Ga_2O_3 phase (space group *C*2/*m*; JCPDS#02-2603).

Hereafter, the 600 °C and 900 °C annealed samples are named as Ga_2O_3_600 and Ga_2O_3_900, respectively. Raman studies have also confirmed the β-Ga_2O_3 phase formation in the annealed sample (see Fig. S1 and related discussion in the ESI†). In previous reports, β-Ga_2O_3 phase formation from the other polymorphous phases was achieved at or above 550 °C.[18,19] Therefore, our findings are in accordance with the reported results and are convincing of the annealing induced β-Ga_2O_3 phase formation in the Ga_2O_3_600 and Ga_2O_3_900 samples. Although the β-Ga_2O_3 phase is present in both of the annealed samples, narrower XRD peaks with a higher intensity are seen in the Ga_2O_3_900 sample. XRD peak intensification in the Ga_2O_3_900 sample is due to the growth of larger sized particles and stabilization of the β-Ga_2O_3 phase under the high-temperature treatment. Larger sized particles and higher crystallinity is clearly seen in the TEM and FFT images of Ga_2O_3_600 and Ga_2O_3_900 samples (see Fig. S2 and related discussion in the ESI†).

XANES studies at the O K-edge, Ga K-edge, Sm L₃-edge, Ga L-edge and Sm M₅,₄-edge

In the case of gallium oxide, the metal d and O 2p states are filled ($3d^{10}$ electronic configuration of Ga^{3+} in Ga_2O_3) and, thus, the final state corresponds to the antibonding orbitals forming from the hybridization of the O 2p state with Ga 4s and Ga 4p.[44–46] Moreover, the overall spectral features of Ga_2O_3 polymorphous are expected to be sensitive to the environment of O atoms with respect to the Ga atoms. Fractional amounts of tetrahedral/octahedral ligand fields of the O atoms in the different phases of Ga_2O_3, which also depends on the Ga site occupancy, may lead to diverse hybridization and crystal field splitting effects. Fig. 2(a) shows the O K-edge XANES of γ-$Ga_{2.67}O_4$, γ-$Ga_{2.67}O_4$: 5Sm and γ-$Ga_{2.67}O_4$: 10Sm nanoparticles. Similarly, Fig. 2(b) shows the O K-edge XANES from the Ga_2O_3_600 and Ga_2O_3_900 samples. The O K-edge spectra can be divided into two regions. The first region is between 530 eV and 545 eV and contains two main features, peak a (533.7 eV) and peak b (538.7 eV). These two features (a and b) correspond to a mixture of O 2p and Ga 4s states and mixture of O 2p and Ga 4p states, respectively.[44–46] The second region in the O K-edge spectra ranges from 545 eV to 570 eV and contains a broad feature at ∼565 eV. The second region is attributed to the pseudo-XAFS oscillations due to multiple scattering effects with the O and surrounding elements. Moreover, the hybridization of O 2p and metal (*n* + 1) sp orbitals is likely to reflect such high energy spectral features in the O K-edge spectra of various oxide compounds.[31–33,43] It is noticeable from Fig. 2(a) that measurable changes are present in the first region of the spectra and negligible changes are seen in the pseudo-XAFS region. The overall intensity of the O K-edge peaks is improved in the γ-$Ga_{2.67}O_4$: 5Sm and γ-$Ga_{2.67}O_4$: 10Sm samples compared with the pure γ-$Ga_{2.67}O_4$ sample. This intensification in the O K-edge features may not due to either the formation of larger sized particles or the existence of trivial oxide phases as our XRD, Raman and TEM results are convincing of a decrease in the size of particles in the Sm doped
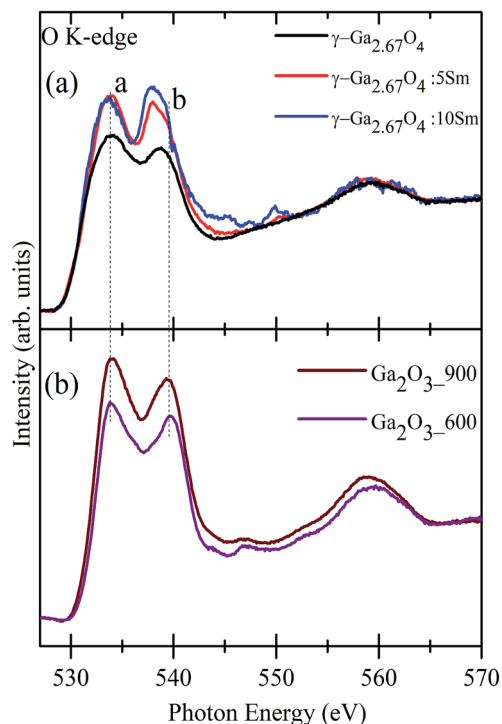
Fig. 2 (a) Normalized O K-edge XANES of (a) γ-$Ga_{2.67}O_4$, γ-$Ga_{2.67}O_4$: 5Sm and γ-$Ga_{2.67}O_4$: 10Sm samples and (b) O K-edge spectra of $Ga_2O_3\_600$ and $Ga_2O_3\_900$ samples. Dotted vertical lines on the peaks a and b indicate the energy position.

Fig. 3 (i) Magnified view of peaks a and b in the O K-edge spectra of pure and Sm doped γ-$Ga_{2.67}O_4$. (ii) Shows the intensity ratio (I_a/I_b) variation as a function of Sm concentration calculated from the O K-edge XANES of pure and Sm doped γ-$Ga_{2.67}O_4$ samples. (iii) Shows a schematic of Ga-O4 tetrahedra with four oxygen ligands surrounding the Ga atom. (iv) Shows the schematic of Ga-O6 octahedra with six oxygen ligands surrounding the Ga atom. (v) Shows a schematic of Sm substitution at the Ga sites and the formation of O vacancies due to the lattice disorders and strain.

samples and have also ruled out the possibility of secondary phase formation. In a previous report, O K-edge XANES of Sm_2O_3 showed an intense peak at ~539 eV due to the O 2p and Sm 5d hybridized orbitals.[47] In the present O K-edge spectra, we have not seen such intense spectral features of Sm_2O_3 and thus we may neglect Sm segregation/trivial phase induced intensification of O K-edge XANES. The observed intensification in the O K-edge features, in the Sm doped samples, suggests that the Sm doped samples have more unoccupied O 2p hybridized orbitals than pure γ-$Ga_{2.67}O_4$. An electron endowment from the O atoms may provide a much-unoccupied density of states with the O 2p hybridized orbitals in the Sm doped compounds. This electronic endowment from the O atoms may result from the various defect formations (O vacancies) and/or distortion in the metal–oxygen polyhedra. While comparing the spectral features of γ-$Ga_{2.67}O_4$: 5Sm and γ-$Ga_{2.67}O_4$: 10Sm samples, it is noticeable that the intensity of the a peak is not much affected but peak b is intensified in the higher Sm concentration doped sample (see Fig. 3(i)). This suggests that the much-unoccupied density of states were made available in the hybridized orbital of O 2p and Ga 4p, rather than the O 2p and Ga 4s hybridized orbitals, upon increasing the Sm concentrations in the γ-$Ga_{2.67}O_4$ lattice. We have considered the variation in the peak a to peak b intensity ratio (*i.e.*, I_a/I_b) from the γ phasic samples (*i.e.*, γ-$Ga_{2.67}O_4$, γ-$Ga_{2.67}O_4$: 5Sm and γ-$Ga_{2.67}O_4$: 10Sm), as shown in Fig. 3(ii). It is evident from Fig. 3(ii) that the I_a/I_b ratio decreases with increasing Sm concentration. Reduction in the I_a/I_b intensity ratio suggests a relative decrease in the electron
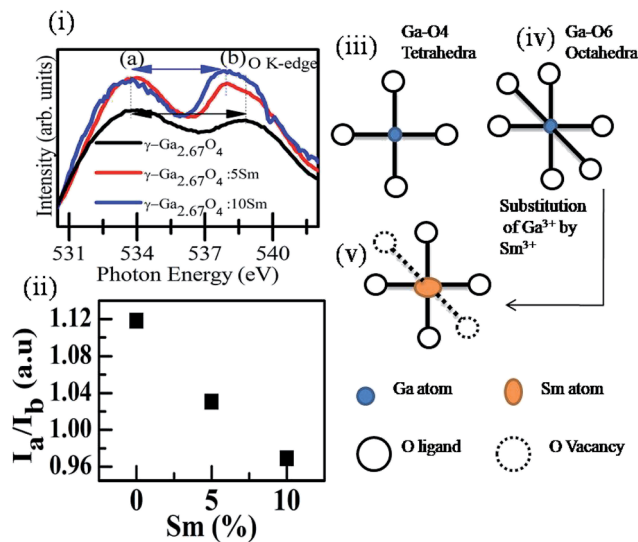
density in the outermost hybrid orbits of O 2p and Ga 4p to that of O 2p and Ga 4s, implying a relative movement of electrons to the inner hybrid orbits with s character from the p character under the distorted crystal lattice of γ-$Ga_{2.67}O_4$: Sm nanoparticles. The I_a/I_b intensity ratio for the β phase samples (*i.e.*, $Ga_2O_3\_600$ and $Ga_2O_3\_900$) is nearly 1.3 and consistent with previous reports.[44–46] However, the overall enhancement in the O K-edge features in the $Ga_2O_3\_900$ sample, compared with the $Ga_2O_3\_600$ sample, could be due to the improved hybridization between the O 2p and Ga 4 s/p orbitals within the larger sized particles of superior crystallinity. Besides the O K-edge peak intensity variation in the Sm doped samples, it is also noticeable that peak b shifts towards a lower photon energy upon Sm doping (see Fig. 3(i); shifting of b peak is shown by the blue coloured arrow). The energy difference between peaks a and b is known as the crystal field splitting energy, Δ_0. The lower energy shifting of peak b indicates that the crystal field splitting is less in the Sm doped nanoparticles compared with pure γ-$Ga_{2.67}O_4$ or β-Ga_2O_3. Moreover, it is also noticeable that Δ_0 is higher (~5.8 eV) for the $Ga_2O_3\_600$ and $Ga_2O_3\_900$ samples compared with the γ-$Ga_{2.67}O_4$ (~4.9 eV). This discrepancy in the Δ_0 of γ-$Ga_{2.67}O_4$ and β-Ga_2O_3 is inherent to the fundamental differences between the crystal/electronic structure of these two polymorphs. The Ga atoms of the monoclinically structured β-Ga_2O_3 form equal proportions of tetrahedra and octahedra with the surrounding O atoms. However, the un-equal site occupancy of Ga atoms in the distorted-spinel structure of γ-$Ga_{2.67}O_4$ may give inappropriate tetrahedra and octahedra ratios.[48,49] It is known that Δ_0 is larger for an octahedral ligand field compared

with a tetrahedral ligand field for a certain oxidation state of the metal element with a definite ligand.[43]

By considering the Δ_0 of the samples, we expect that the fractional occupancy of Ga atoms at tetrahedral sites is larger in the case of γ-Ga$_{2.67}$O$_4$ polymorphs and the octahedral sites are the favourable sites of Ga atoms in the β phasic samples. In a previous study, the preferred octahedral sites occupancy for the dopants were reported in spinel phase MnFe$_2$O$_4$ nanoparticles.[50]

Here, we may hypothesize that the Sm doping in the γ-Ga$_{2.67}$O$_4$ lattice offers more tetrahedral sites to the metal atoms at the expense of octahedral sites. Under the condition of substitutional doping of Sm at the Ga sites, if we assume that isovalent Sm^{3+} ions take the octahedral sites of Ga^{3+} ions, O vacancies are expected to form because of the disorder/strain produced *via* imbalance of ionic radii and electronegativity of Sm^{3+} and Ga^{3+} ions. Formation of O vacancies has also been reported in the isovalent (*i.e.*, Sn^{4+}, Hf^{4+} and Zr^{4+}) element doped CeO$_2$ nanoparticles (Ce^{4+} ions in CeO$_2$), and was ascribed to the imbalance of ionic radii and lattice distortion.[32,33,51] In the case of Ga-O4 tetrahedra, there are only four O ligand approaches to the Ga atoms (see the schematic in Fig. 3(iii)). Similarly, six O ligands form Ga-O6 octahedra with the Ga atoms (see the schematic in Fig. 3(iv)). Reduction of metal-O6 octahedra into metal-O4 tetrahedra is possible *via* O vacancy formation and is shown in the Fig. 3(v). Further analysis at Ga K-edge XANES and EXAFS is helpful to elaborate such a hypothesis of an increase in the metal-O4 tetrahedral sites and decrease in the metal-O6 octahedral sites in the Sm doped γ-Ga$_{2.67}$O$_4$ and is discussed in the following sections.

The Ga K-edge XANES originates from the 1s → 4p transitions and can be used for understanding the inconsequential local electronic structure differences among the polymorphous Ga$_2$O$_3$ compounds.[48,49,52–54] Fig. 4(a) shows the Ga K-edge XANES spectra of γ-Ga$_{2.67}$O$_4$, γ-Ga$_{2.67}$O$_4$: 5Sm and γ-Ga$_{2.67}$O$_4$: 10Sm samples while Fig. 4(c) shows the second derivates of the Ga K-edge XANES spectra. Here, we have analysed the Ga K-edge XANES spectra by concerning the two aspects; (i) valence state change of Ga^{3+} ions and (ii) perturbation in the Ga lattice site occupancy (*i.e.*, change in the Ga-O6 octahedra and Ga-O4 tetrahedra proportions), if any, upon Sm doping or annealing conditions. The edge-energy position and other spectral features of the pure and Sm doped γ-Ga$_{2.67}$O$_4$ samples fairly match each other (can be seen in the second derivate spectra) and nullify any valence state change upon Sm doping. Similar to the Ga K-edge XANES, the Sm L-edge XANES spectra and second derivate spectra of the γ-Ga$_{2.67}$O$_4$: 5Sm and γ-Ga$_{2.67}$O$_4$: 10Sm samples do not show any noteworthy changes and, thus, the possibility of valence state change of Sm ions can be neglected. The Ga K-edge and Sm L-edge XANES results were further cross-checked with the Ga L-edge and Sm M$_{5,4}$-edge XANES and convey the +3 valence state of Ga and Sm ions (see Fig. S3 and S4 in the ESI† and discussion therein). Sm L-edge and Sm M-edge XANES are convincing of Sm^{3+} ions in the samples but the existence of Sm at the surface/grain boundaries of NPs may not be explained within the periphery of the XANES results. Interesting spectral changes were observed in the Ga K-edge XANES
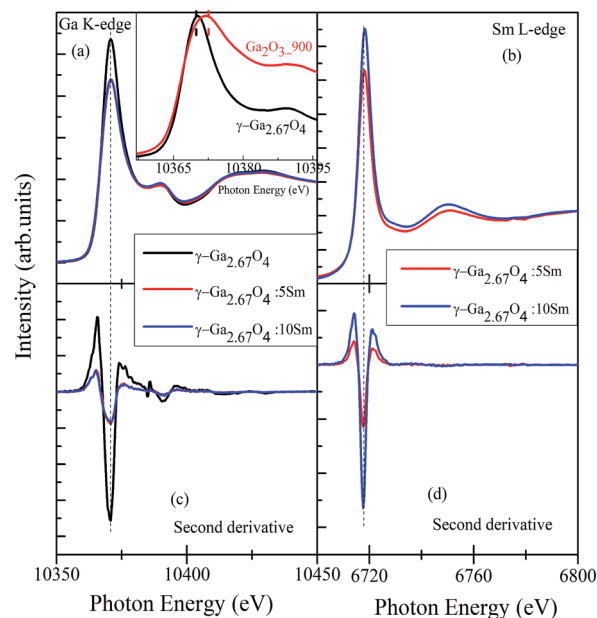

Fig. 4 (a) and (b) show the Ga K-edge and Sm L$_3$-edge XANES spectra, respectively. The lower panels (c) and (d) are the second derivative spectra of the Ga K-edge and Sm L-edge, respectively. Inset of (a) shows a comparison of the white-line peaks of the γ-Ga$_{2.67}$O$_4$ and Ga$_2$O$_3$_900 samples.

spectra, while we have analysed the white-line region of γ-Ga$_{2.67}$O$_4$ and Ga$_2$O$_3$_900 samples, by normalizing the white-line peak intensity (see the inset of Fig. 4(a)). It is evidenced from the figure that the Ga$_2$O$_3$_900 sample (*i.e.*, β-Ga$_2$O$_3$ phase) exhibits a broad white line peak compared with the sharp peak in γ-Ga$_{2.67}$O$_4$. It seems that the white-line peak position of the β-Ga$_2$O$_3$ sample is at a slightly higher energy (~2.2 eV) compared with the γ-Ga$_{2.67}$O$_4$ sample. It is known for the transition metal compounds that the edge-energy and white-line peak position progressively shift towards a higher energy with increasing valence state (cation charge) of metal ions.[55] In the present study, the edge-energy positions are nearly identical; however, the white line peak positions give the impression of positive energy shifting for the β-Ga$_2$O$_3$ compound with respect to γ-Ga$_{2.67}$O$_4$. In a previous report, the Al K-edge XANES also showed white-line peak shifting towards a higher energy with an increase of the oxygen coordination number of Al from 4 to 6 (*i.e.*, sodalite to kyanite transformation).[56] Similarly, a Ga K-edge XANES spectrum of α-Ga$_2$O$_3$ has been reported with a +2 eV shifting in the white-line peak position with respect to GaAs despite the same valence state of the Ga ions (*i.e.*, Ga^{3+}) in both of the compounds.[52] The existence of a higher energy white-line peak in α-Ga$_2$O$_3$ and a lower energy white-line peak in GaAs was ascribed to the diverse site occupancy of Ga atoms.[48,52] In the GaAs compound, the Ga atoms occupy regular tetrahedral sites, whereas in α-Ga$_2$O$_3$ the Ga atoms are in distorted octahedral sites.[52] By considering the previous reports and findings of our Ga K-edge XANES, the low energy white-line peak in the present study of γ-Ga$_{2.67}$O$_4$ sample can be anticipated as a favourable tetrahedral occupancy of Ga atoms, whereas the broadened or positive energy shifted white-line peak in the Ga$_2$O$_3$_900 sample

may be an indication of mixed occupancy of the Ga atoms at tetrahedral and octahedral sites.

To understand the quantitative Ga occupancy in $Ga_2O_3\_900$, γ-$Ga_{2.67}O_4$, and Sm doped γ-$Ga_{2.67}O_4$, we have deconvoluted the white line peak of Ga K-edge XANES and present it in Fig. 5(a–d). The deconvolution was done by assuming the two components in the main peak region (i.e., 10 355 eV to 10 385 eV) and the fittings were done by applying the Gaussian curve fitting method.[48,49] The details of the fitting procedure and the other parameters like peak energy, full width at half maxima of the peaks and the fractional percentages of tetrahedral and octahedral Ga atoms (i.e., Ga(t)% and Ga(o)%) in various samples are provided in Table S1 of the ESI.† According to previous reports,[48,49,52] the Gaussian 1 (magenta colour) and Gaussian 2 (olive colour) in Fig. 5 can be regarded as the contribution from the tetrahedral (Ga(t)) and octahedral (Ga(o)) occupancy of Ga atoms, respectively. The integrated areas of Gaussian 1 and Gaussian 2 have been applied to determine the fractional percentage of Ga(t) and Ga(o) from various samples. Detailed calculations are provided in the ESI.† Our calculations convey that the $Ga_2O_3\_900$ sample exhibits 48.4% and 51.6% of Ga(t) and Ga(o) atoms, respectively (i.e., Ga(t)/Ga(o) ratio of ~0.92). In previous studies, a 1 : 1 ratio of Ga(t) : Ga(o) has been reported for the commercial β-Ga_2O_3 compound.[48,49] A slightly smaller Ga(t) : Ga(o) ratio from the $Ga_2O_3\_900$ sample may be due to the

higher occupancy of Ga atoms on octahedral sites. On the other hand, the γ-$Ga_{2.67}O_4$ sample has shown 58.8% and 41.2% fractional percentages of Ga(t) and Ga(o), respectively (i.e., Ga(t)/Ga(o) ratio of ~1.4). Ga(t)/Ga(o) ratios were further increased for the γ-$Ga_{2.67}O_4$: 5Sm (~1.51) and γ-$Ga_{2.67}O_4$: 10Sm (~1.62) samples. The highest Ga(t)/Ga(o) ratio was reported to be ~1.8 for the poorly crystalline and small sized Ga_2O_3 samples[48] and is in agreement with our results. Ga K-edge XANES results imply that the γ phasic samples have preferred tetrahedral sites of Ga species and the substitution of Sm leads to much octahedral site deformation. Population of Ga atoms at tetrahedral (Ga-O4) sites at the expense of octahedral (Ga-O6) sites may facilitate O ion vacancy in the γ-$Ga_{2.67}O_4$ lattice leading to more unoccupied O 2p hybridized orbitals in the Sm doped samples, as illustrated in the O K-edge XANES. The smaller Δ_0 in the O K-edge spectra is analogous to the higher Ga(t) : Ga(o) ratio for the pure and Sm doped samples and is convincing of the higher metal-O4 tetrahedra in the γ-$Ga_{2.67}O_4$, γ-$Ga_{2.67}O_4$: 5Sm and γ-$Ga_{2.67}O_4$: 10Sm samples, compared with β-Ga_2O_3.

EXAFS study at Ga K-edge

In order to get a further understanding of the local structure differences among the pure γ-$Ga_{2.67}O_4$, β-Ga_2O_3 and Sm doped γ-$Ga_{2.67}O_4$ samples, systematic Ga K-edge EXAFS data are investigated by applying the ATHENA-ARTEMIS and FEFF calculations.[57,58] Details of the EXAFS data simulations are provided in the ESI.† The spectra presented in the Fig. 6 are not corrected for phase shift; however, phase-corrected spectra are provided in the ESI.† The $\chi(R)$ vs. R spectrum of $Ga_2O_3\_900$ sample shows a distinct doublet in the first oscillation of the Ga–O shell; however, the pure and Sm doped γ-$Ga_{2.67}O_4$ samples are likely to have one oscillation in the Ga–O shell. During the simulations, individual oscillations from the tetrahedrally coordinated Ga and octahedrally coordinated Ga were examined and exhibit bond lengths of ~1.85 Å and ~1.99 Å for the Ga–O shells of the tetrahedral and octahedral coordinated Ga atoms, respectively. Similarly, a sharp oscillation at 3.0 Å and a mild oscillation at 3.3 Å were also observed due to the octahedral and tetrahedral Ga–Ga shells, respectively. The appearance of such features in the $Ga_2O_3\_900$ sample is characteristic of the β-Ga_2O_3 phase and is due to contributions from the tetrahedrally and octahedrally coordinated Ga atoms in this sample.[48,49] After accreting the contributions from both of the individual oscillations from tetrahedrally and octahedrally coordinated Ga, the experimental spectra were fairly simulated for the $Ga_2O_3\_900$ sample (see Fig. 6(a) and (e)). The simulated structural parameters (see Table 1) show that there are two Ga–O bond distances (i.e., 1.82 Å and 1.92 Å) for the tetrahedral and octahedral occupation of Ga, respectively. In previous reports, the average Ga–O bond distance for the β-Ga_2O_3 phase is reported to be 1.83 Å for the tetrahedrally coordinated Ga atoms and 2.0 Å for the octahedrally coordinated Ga atoms.[48,49] Our simulated results for the $Ga_2O_3\_900$ sample are in fair agreement with the previously reported EXAFS results for β-Ga_2O_3, thus confirming our XRD and Raman results on the formation of a β-Ga_2O_3 phase in this sample.
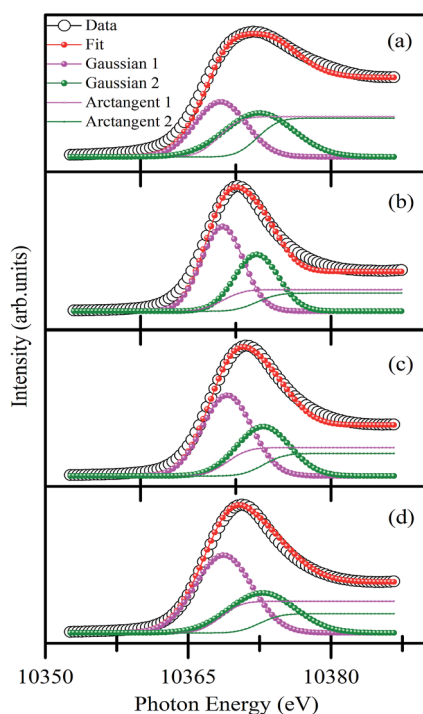

Fig. 5 Deconvolution of the Ga K-edge white line peak of (a) $Ga_2O_3\_900$, (b) γ-$Ga_{2.67}O_4$, (c) γ-$Ga_{2.67}O_4$: 5Sm and (d) γ-$Ga_{2.67}O_4$: 10Sm samples. Gaussian 1 and Gaussian 2 represent the tetrahedral and octahedral contributions, respectively. Arctangent 1 and arctangent 2, which were assigned for the continuum absorption, correspond to Gaussian 1 and Gaussian 2, respectively. The energy of the inflection point of the arctangent curve is taken to be the same as that of the corresponding Gaussian curve.
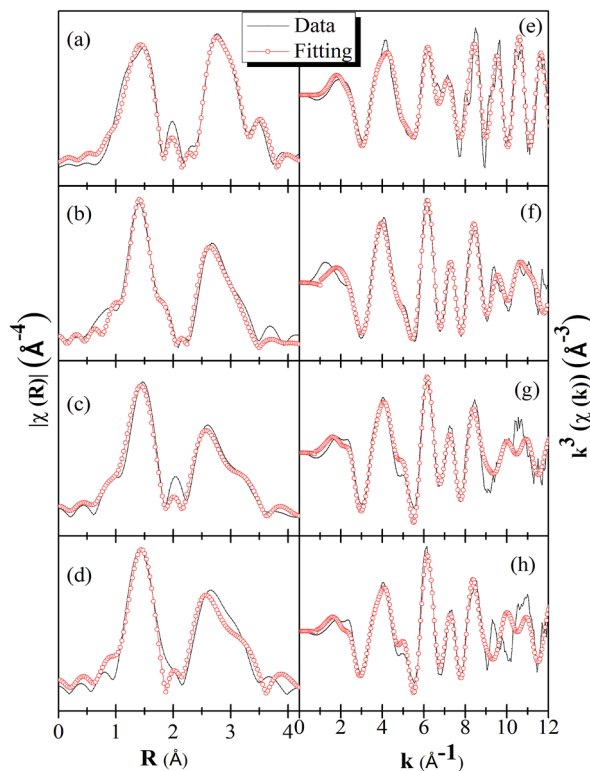
Fig. 6 $\chi(R)$ *vs.* R spectra of (a) $Ga_2O_3\_900$, (b) γ-$Ga_{2.67}O_4$, (c) γ-$Ga_{2.67}O_4$: 5Sm and (d) γ-$Ga_{2.67}O_4$: 10Sm, respectively. $\chi(k)$ *vs.* k spectra of (e) $Ga_2O_3\_900$, (f) γ-$Ga_{2.67}O_4$, (g) γ-$Ga_{2.67}O_4$: 5Sm and (h) γ-$Ga_{2.67}O_4$: 10Sm, respectively. The spectra are not corrected for phase shift.

It is also noticeable from Fig. 6(b) that the intensity of the Ga–Ga shell (between the 2–3.4 Å) is quite smaller than that of the Ga–O shell intensity, while it was quite comparable with that of the $Ga_2O_3\_900$ sample. This is due to the fact that the

$Ga_2O_3\_900$ sample has a high crystallinity and larger particle size compared with the γ-$Ga_{2.67}O_4$ sample. Diminishing the Ga–Ga shell intensity in Fig. 6(c and d), for the γ-$Ga_{2.67}O_4$: Sm samples, could be related to the net decrease in the nanoparticle size and increase in the amorphous content in the samples. In previous reports, a continuous decrease in the EXAFS oscillations with a decrease in the nanoparticle size is also reported.[59] It is noticeable from Table 1 that the Ga–O and Ga–Ga bond distances are longer for the Sm doped sample compared with pure $Ga_{2.67}O_4$. The net increase in the Ga–O or Ga–Ga bond distances is, certainly, due to the structural perturbation in the crystalline lattice of gallium oxide upon Sm^{3+} ion doping. In the XRD studies, we have noticed an enlargement of $d_{(311)}$ values for the Sm^{3+} ion doped samples. Thus, the enlarged Ga–O and Ga–Ga bond distances are the consequences of the insertion of larger Sm^{3+} ions at the lattice position of Ga^{3+} ions. In previous reports,[48,49] Ga–O shell coordination numbers were applied to calculate the fractional Ga(t) and Ga(o). We have also evaluated the Ga(t)/Ga(o) = $(N/4)/(N/6)$ ratio from the coordination number of Ga–O shell.[48] It is noticeable from Table 1 that the Ga(t)/Ga(o) ratios, for all of the samples, are nearly the same as obtained from the Ga K-edge XANES. In the previous EXAFS analysis,[48] the maximum Ga(t)/Ga(o) ratio was evaluated to be ~1.7 for the poorly crystalline and small sized (2–6 nm) Ga_2O_3 NP samples and is in accordance with our findings. Our XANES and EXAFS results are, thus, convincing of favourable tetrahedral sites of the Ga atoms in γ-$Ga_{2.67}O_4$ which are further increased in the Sm doped samples leading to higher Ga(t)/Ga(o) ratios.

Photoluminescence study

Ga_2O_3 is known as the widest band gap material ($E_g \approx 4.8$ eV) among all of the known transparent conducting oxides. Its semiconducting nature originates from the shallow donor states caused by native defects.[18–23] The photoluminescence

Table 1 Structural parameters obtained from the Ga K-edge EXAFS data simulations. N (coordination number), R (bond length), σ^2 (Debye–Waller factor), E_0 (edge-energy correction) and Ga(t)/Ga(o) (tetrahedral/octahedral ratio of Ga sites). Ga_o and Ga_t represent the octahedral and tetrahedral sites of Ga, respectively. The numbers in parentheses represent error therein. The Ga(t)/Ga(o) ratio is calculated by the following equation: Ga(t)/Ga(o) = $(N/4)/(N/6)$

Name	Ga sites	Shell	N	R (Å)	σ^2 (Å^2)	E_0 (eV)	Ga(t)/Ga(o)
$Ga_2O_3\_900$	Ga_o	Ga–O	5.4	1.92(3)	0.012(2)	3.0	0.85
		Ga–Ga	5.4	3.09(3)	0.009(5)		
	Ga_t	Ga–O	3.0	1.82(7)	0.047(0)		
		Ga–Ga	6.1	3.34(7)	0.008(0)		
γ-Ga_2O_3	Ga_o	Ga–O	4.1	2.01(7)	0.026(4)	2.5	1.17
		Ga–Ga	4.7	2.97(1)	0.007(4)		
	Ga_t	Ga–O	3.2	1.85(0)	0.002(0)		
		Ga–Ga	5.7	3.34(2)	0.012(4)		
γ-Ga_2O_3 : 5Sm	Ga_o	Ga–O	3.7	2.04(9)	0.011(8)	2.2	1.37
		Ga–Ga	3.9	3.01(4)	0.008(9)		
	Ga_t	Ga–O	3.4	1.90(8)	0.007(1)		
		Ga–Ga	5.1	3.45(0)	0.047(0)		
γ-Ga_2O_3 : 10Sm	Ga_o	Ga–O	3.5	2.06(9)	0.038(5)	2.7	1.59
		Ga–Ga	3.5	3.11(3)	0.007(0)		
	Ga_t	Ga–O	3.3	1.92(7)	0.004(8)		
		Ga–Ga	4.5	3.46(9)	0.018(8)		

from this compound is also a matter of debate and has been understood on the basis of donor–acceptor pair (DAP) recombination.[60–62] Yet, the exact nature of the localized donor and acceptor sites is under investigation. It is considered that the acceptor is a gallium–oxygen vacancy pair $[(V_o, V_{Ga})^\times]$ and the donor is an oxygen vacancy $(V_o^\times)$. After illuminating the Ga_2O_3 with sufficient energy of photons, an electron with the donor and a hole with the acceptor level can be generated with a blue-green emission; however, particle size dependence[60] can be achieved according to the relation,[61] $V_o^\times + (V_o, V_{Ga})^\times \rightarrow (V_o, V_{Ga})' + V_o^. + h\nu$. Fig. 7 shows the room temperature PL spectrum of (a) γ-$Ga_{2.67}O_4$, (b) γ-$Ga_{2.67}O_4$: 5Sm (c) γ-$Ga_{2.67}O_4$: 10Sm, (d) $Ga_2O_3\_600$ and (e) $Ga_2O_3\_900$ samples. In the previous reports, an intense blue emission has been reported from the γ-Ga_2O_3 colloidal nanoparticles.[60,61] In the present study, the γ-$Ga_{2.67}O_4$ nanoparticles exhibit a dominating emission centred at $\sim$520 nm (cyan-green) with a significant band at $\sim$434 nm (violet-blue emission). This may be due to the fact that γ-$Ga_{2.67}O_4$ nanoparticles contain a lower concentration of Ga and O vacancy sites, compared with the previously reported Ga_2O_3 colloidal nanoparticles, providing a lower number of DAPs (attributed to the lower PL intensity of the violet-blue band) and a larger average energy separation between the recombining pairs or lower Coulomb interaction between the donor and acceptor sites (attributed to cyan-green PL).

While comparing the PL spectra of γ-$Ga_{2.67}O_4$ nanoparticles and the annealed samples ($Ga_2O_3\_600$ and $Ga_2O_3\_900$), it is noticeable that the annealed samples show a dominating green emission at $\sim$548 nm and a negligible blue emission band. The red shift in the PL spectra, comparing with pure γ-$Ga_{2.67}O_4$, indicates a smaller average energy separation between the
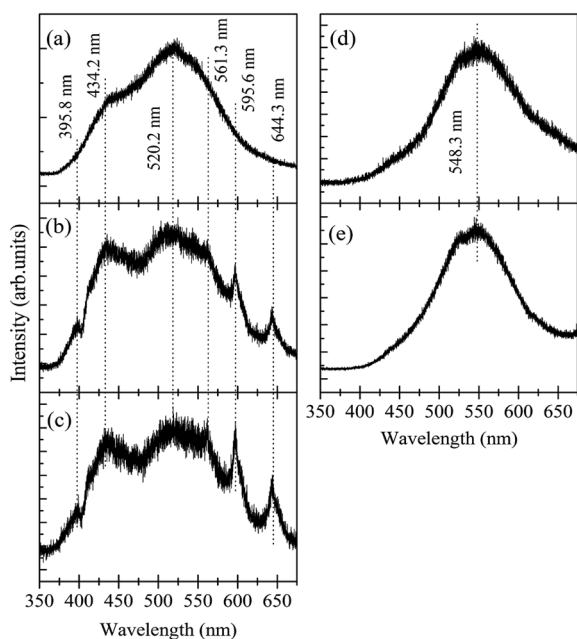
recombining pairs in the annealed samples. The annealing induced ripening and fusion of particles, as evidenced in the TEM study, may have hidden the surface defect induced shallow energy levels in the energy gap of the material, leading to the quenching of the blue emission from the $Ga_2O_3\_600$ and $Ga_2O_3\_900$ samples. Only the interior defects $([(V_o, V_{Ga})^\times]$ or $(V_o^\times))$, which have a smaller energy separation of donor–acceptor pairs or more Coulomb interactions, are expected to be responsible for the green emission from the $Ga_2O_3\_600$ and $Ga_2O_3\_900$ samples. An interesting variation can be seen in the PL spectra of Sm doped samples: (i) a low-intensity band evolves in the deep violet region ($\sim$396 nm), (ii) the intensity of the $\sim$434 nm band is increased and (iii) intense bands appear between 550 nm and 675 nm. Taken together, XRD, XAS and PL data indicate that Sm doping in γ-$Ga_{2.67}O_4$ nanoparticles causes a change in DAP recombination because of several factors: (i) a decrease in the average particle size, which provides more surface related defect states,[63] (ii) alteration in the Ga and O local lattice site occupancy, which gives diverse defect levels in the compound[18–20] and (iii) the existence of the Sm^{3+} ion in the γ-$Ga_{2.67}O_4$ lattice, which provides distinct defect states and intra-4f transitions.[64,65] The broad range of luminescence from the γ-$Ga_{2.67}O_4$: Sm nanoparticles can be understood by knowing the energy and charge transfer process in distinct electronic states.

In Fig. 8, we present a schematic of the DAP and Sm^{3+} ion transition induced luminescence in the γ-$Ga_{2.67}O_4$: Sm nanoparticles. Excitation by the 325 nm wavelength from a He–Cd laser leads to electronic transitions and trapping of photo excited electrons and holes in the donor and acceptor states, respectively. Recombination of electrons and holes leads to typical emission spectra from γ-$Ga_{2.67}O_4$ nanoparticles. The energy (or colour) of emitted radiation is governed by the coulombic interaction between the charge donor and acceptors and can be expressed as;[60–62] $E = E_g - (E_{donor} + E_{acceptor}) + E_{coulombic} \pm nE_{phonon}$. Here, E_g is the band gap energy of the material, E_{donor} and $E_{acceptor}$ are the donor and acceptor binding
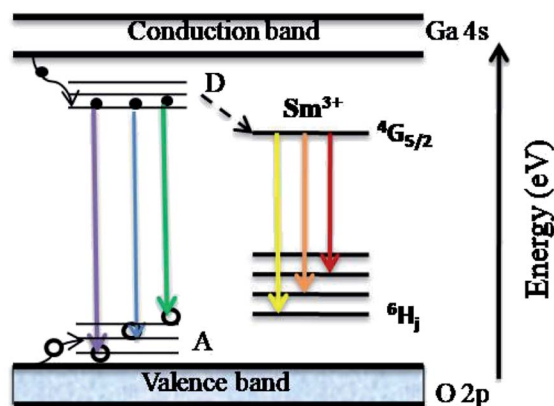

Fig. 7 Room temperature PL spectra of (a) pure γ-$Ga_{2.67}O_4$, (b) γ-$Ga_{2.67}O_4$: 5Sm, (c) γ-$Ga_{2.67}O_4$: 10Sm, (d) $Ga_2O_3\_600$ and (e) $Ga_2O_3\_900$ samples.

Fig. 8 Schematic representation of the charge and energy transfer processes involved in the luminescence characteristics of Sm^{3+} doped γ-$Ga_{2.67}O_4$ nanoparticles. The solid spheres and open circles represent electrons and holes, respectively. D and A correspond to the defect induced formation of donor and acceptor bands, respectively.

energies, respectively. The E_{phonon} term represents the energies of phonons involved in the radiative transitions and the coulombic interaction term ($E_{coulombic} = e^2/4\pi\varepsilon r$) is the deciding term for the emitted energy (or colour) from a DAP transition. Since the average donor–acceptor separation (r) becomes narrower for the smaller sized particles,[60–62] a higher emission energy can be expected from the above relation for a smaller sized particle. The observed violet emission ($\sim$395.5 nm) and increased intensity of the $\sim$434 nm band in the Sm doped samples may be the consequence of an Sm doping induced decrease of particle size and increase in the defect concentration. Our O K-edge and Ga K-edge XANES/EXAFS are convincing of O and Ga defect formation and Ga lattice site occupancy alteration upon the insertion of Sm^{3+} ions. These kinds of defect states are certainly responsible for the intensification of the $\sim$434 nm band.

Donor and acceptor states not only provide DAP induced radiative transitions but also play a role in the sensitization of the Sm emission by nonradiative transfer of the DAP exciton energy to the doped rare earth ions (shown by a dashed black line in Fig. 8).[12] The 4f electrons of rare-earth ions in the host materials are quite similar to the free ions and the emission characteristics are determined by the crystalline fields of the host compound around the rare-earth ions.[12,64] In several reports, the 3+ valence state of rare-earth ions was reduced to 2+, even under *in situ* XAS data collection, leading to intriguing electronic structure and luminescence properties.[12,65] In the present study, our Sm L-edge and Sm $M_{5,4}$-edge XANES, along with the multiplet calculations, have confirmed Sm^{3+} ions in the samples, and therefore Sm^{3+} reduction into Sm^{2+} can be neglected and the observed luminescence properties are the consequences of defect formation and the Sm^{3+} ion related $^4G_{5/2} \rightarrow {}^6H_j$ transition induced emission properties. Despite the enhancement in the defect induced luminescence bands (violet-

blue-green bands) the intensity of the Sm^{3+} ions induced transitions,[64,65] $^4G_{5/2} \rightarrow {}^6H_{5/6}$ (yellow emission), $^4G_{5/2} \rightarrow {}^6H_{7/6}$ (orange emission) and $^4G_{5/2} \rightarrow {}^6H_{9/6}$ (red emission), are also enhanced, conveying that the luminescence properties of γ-$Ga_{2.67}O_4$ can be engineered by the formation of controlled defect states and incorporation of variable Sm^{3+} ion concentration. The photoluminescence spectra of the samples were converted to the Commission International de I'Eclairage (CIE-1913) chromaticity diagram and are presented in the Fig. 9. It is visible from the CIE colour chromaticity diagram that the pure γ-$Ga_{2.67}O_4$ nanoparticle sample exhibits DAP induced cyan-green emission characteristics (CIE coordinates, 0.26, 0.43) while the Ga_2O_3_600 (CIE coordinates, 0.36, 0.45) or Ga_2O_3_900 (CIE coordinates, 0.37, 0.46) samples exhibits green yellow emission which is analogous to the previous reports where the increase of particle size had demonstrated the red-shifted PL bands.[60,61] By considering the standard CIE coordinates for the white light (*i.e.*, 0.333, 0.333),[66] we can state that the Sm doped γ-$Ga_{2.67}O_4$ nanoparticles have shown a nearly white line emission, *i.e.*, ranging from violet-blue to orange-red emission. The CIE coordinates for the γ-$Ga_{2.67}O_4$: 5Sm and γ-$Ga_{2.67}O_4$: 10Sm samples are (0.28, 0.34) and (0.30, 0.35), respectively.

Conclusions

Specifically, the non-aqueous synthesis with hydrazine monohydrate has helped us to fabricate the barely reported and metastable γ-$Ga_{2.67}O_4$ nanoparticles in the present study. XRD and Raman results are convincing of the single phase nature of the as-prepared and annealed samples. XRD and TEM studies signify a particle size reduction and poor crystallinity in the Sm doped samples. Ga K/L-edge and Sm $L_3/M_{5,4}$-edge XANES have confirmed Ga^{3+} and Sm^{3+} ions in the samples and have also ruled out the valence reduction of metal ions under the Sm doping and annealing conditions. O K-edge XANES has shown a systematic increase in the intensity of O 2p and Ga 4s/4p hybridized orbitals and decrease in the crystal field splitting energy upon increasing the Sm concentration in the γ-$Ga_{2.67}O_4$ lattice. Detailed analysis at the Ga K-edge XANES and EXAFS data has conveyed a $\sim$0.9 Ga(t)/Ga(o) ratio in the β-Ga_2O_3 phase, signifying a higher proportion of Ga-O6 octahedra. Pure γ-$Ga_{2.67}O_4$ and Sm doped γ-$Ga_{2.67}O_4$ samples have exhibited higher Ga(t)/Ga(o) ratios and signify the higher Ga-O4 tetrahedra proportions. Photoluminescence spectra and CIE diagrams have shown that the γ-$Ga_{2.67}O_4$ phase has exhibited DAP induced cyan-green emission. The Sm incorporation into the γ-$Ga_{2.67}O_4$ lattice has offered a wide range of emission, with CIE coordinates closer to that of white light, ranging from violet-blue to orange-red. The results of this research work provide a guideline for the preparation and understanding of the metastable phase of gallium oxide, which is not only interesting for its local atomic/electronic structure properties but also exhibits a wide range of emission characteristics upon Sm doping.

Fig. 9 CIE colour chromaticity diagram of sample 1 (pure γ-$Ga_{2.67}O_4$), sample 2 (γ-$Ga_{2.67}O_4$: 5Sm), sample 3 (γ-$Ga_{2.67}O_4$: 10Sm), sample 4 (Ga_2O_3_600) and sample 5 (Ga_2O_3_900).

Conflicts of interest

There are no conflicts to declare.

Acknowledgements

Notes and references

1 R. Roy, V. G. Hill and E. F. Osborn, *J. Am. Chem. Soc.*, 1952, **74**, 719.

2 S. Yoshioka, H. Hayashi, A. Kuwabara, F. Oba, K. Matsunaga and I. Tanaka, *J. Phys.: Condens. Matter*, 2007, **19**, 346211.

3 H. Y. Playford, A. C. Hannon, E. R. Barney and R. I. Walton, *Chem.–Eur. J.*, 2013, **19**, 2803.

4 H. Y. Playford, A. C. Hannon, M. G. Tucker, D. M. Dawson, S. E. Ashbrook, R. J. Kastiban, J. Sloan and R. I. Wolton, *J. Phys. Chem. C*, 2014, **118**, 16188.

5 M. Passlack, E. F. Schubert, W. S. Hobson, M. Hong, N. Moriya, S. N. G. Chu, K. Konstadinidis, J. P. Mannaerts, M. L. Schnoes and G. J. Zydzik, *J. Appl. Phys.*, 1995, **77**, 686.

6 L. Mazeina, F. Keith Perkins, V. M. Bermudez, S. P. Arnold and S. M. Prokes, *Langmuir*, 2010, **26**, 13722.

7 D. Fracasso, M. I. Muglali, M. Rohwerder, A. Terfort and R. C. Chiechi, *J. Phys. Chem. C*, 2013, **117**, 11367.

8 V. Ghodsi, S. Jin, J. C. Byers, Y. Pan and P. V. Radovanovic, *J. Phys. Chem. C*, 2017, **121**, 9433.

9 X. S. Wang, J. Q. Situ, X. Y. Ying, H. Chen, H. F. Pan, Y. Jin and Y. Z. Du, *Acta Biomater.*, 2015, **22**, 164.

10 R. Lorenzi, A. Paleari, N. V. Golubev, E. S. Ignateva, V. N. Sigaev, M. Niederberger and A. Lauria, *J. Mater. Chem. C*, 2015, **3**, 41.

11 T. Wang and P. V. Radovanovic, *J. Phys. Chem. C*, 2011, **115**, 18473.

12 A. Layek, B. Yildirim, V. Ghodsi, L. N. Hutfluss, M. Hegde, T. Wang and P. V. Radovanovic, *Chem. Mater.*, 2015, **27**, 6030.

13 H. He, R. Orlando, M. A. Blanco and R. Pandey, *Phys. Rev. B*, 2006, **74**, 195123.

14 M. Mohamed, C. Janowitz, I. Unger, R. Manzke, Z. Galazka, R. Uecker, R. Fornari, J. R. Weber, J. B. Varley and C. G. Van de Walle, *Appl. Phys. Lett.*, 2010, **97**, 211903.

15 Y. Jinliang and Q. Chong, *J. Semicond.*, 2016, **37**, 042002.

16 N. T. Son, K. Goto, K. Nomura, Q. T. Thieu, R. Togashi, H. Murakami, Y. Kumagai, A. Kuramata, M. Higashiwaki, A. Koukitu, S. Yamakoshi, B. Monemar and E. Janzén, *J. Appl. Phys.*, 2016, **120**, 235703.

17 X. Qiu, J. Zhang, H. Dong and X. Zhou, *Theor. Chem. Acc.*, 2017, **136**, 79.

18 S. Ye, Y. Zhang, H. He, J. Qiu and G. Dong, *J. Mater. Chem. C*, 2015, **3**, 2886.

19 C. C. Huang and C. S. Yeh, *New J. Chem.*, 2010, **34**, 103.

20 B. K. Kang, S. R. Mang, D. H. Go and D. H. Yoon, *Mater. Lett.*, 2013, **111**, 67.

21 E. I. EL-Sayed, A. A. Al-Ghamdi, S. Al-Heniti, F. Al-Marzouki and F. El-Tantawy, *Mater. Lett.*, 2011, **65**, 317.

22 C. T. Shao, W. Z. Lang, X. Yan and Y. J. Guo, *RSC Adv.*, 2017, **7**, 4710.

23 K. Shimura and H. Yoshida, *Phys. Chem. Chem. Phys.*, 2012, **14**, 2678–2684.

24 D. Chiche, M. Digne, R. Revel, C. Chanéac and J. P. Jolivet, *J. Phys. Chem. C*, 2008, **112**, 8524.

25 A. Sharma, M. Varshney, K. H. Chae, H. J. Shin and S. O. Won, *Curr. Appl. Phys.*, 2016, **16**, 1326.

26 L. M. Moreau, D. H. Ha, H. Zhang, R. Hovden, D. A. Muller and R. D. Robinson, *Chem. Mater.*, 2013, **25**, 2394.

27 P. Thakur, R. Kumar, J. C. Cezar, N. B. Brookes, A. Sharma, S. K. Arora, S. Gautam, A. Kumar, K. H. Chae and I. V. Shvets, *Chem. Phys. Lett.*, 2011, **501**, 404.

28 S. Gautam, S. N. Kane, B. G. Park, J. Y. Kim, L. K. Varga, J. H. Song and K. H. Chae, *J. Non-Cryst. Solids*, 2011, **357**, 2228.

29 A. Lussier, J. Dvorak, Y. U. Idzerda, S. B. Ogale, S. R. Shinde, R. J. Choudary and T. Venkatesan, *J. Appl. Phys.*, 2004, **95**, 7190.

30 A. Sharma, A. P. Singh, P. Thakur, N. B. Brookes, S. Kumar, C. G. Lee, R. J. Choudhary, K. D. Verma and R. Kumar, *J. Appl. Phys.*, 2010, **107**, 093918.

31 W. C. Wang, S. Y. Chen, P. A. Glans, J. Guo, R. Chen, K. W. Fong, C. L. Chen, A. Gloter, C. Lin Chang, T. S. Chan, J. M. Chen, J. F. Leed and C. L. Dong, *Phys. Chem. Chem. Phys.*, 2013, **15**, 14701–14707.

32 A. Sharma, M. Varshney, H. J. Shin, Y. J. Park, M. G. Kim, T. K. Ha, K. H. Chae and S. Gautam, *Phys. Chem. Chem. Phys.*, 2014, **16**, 19909.

33 A. Sharma, M. Varshney, J. H. Park, T. K. Ha, K. H. Chae and H. J. Shin, *Phys. Chem. Chem. Phys.*, 2015, **17**, 30065.

34 X. Tan, T. Yao, R. Long, Z. Sun, Y. Feng, H. Cheng, X. Yuan, W. Zhang, Q. Liu, C. Wu, Y. Xie and S. Wei, *Sci. Rep.*, 2012, **2**, 466.

35 A. Sharma, M. Varshney, H. J. Shin, K. H. Chae and S. O. Won, *Spectrochim. Acta, Part A*, 2017, **173**, 549.

36 Y. Wu, L. Fan, W. Huang, S. Chen, S. Chen, F. Chen, C. Zou and Z. Wu, *Phys. Chem. Chem. Phys.*, 2014, **16**, 17705.

37 A. Sharma, M. Varshney, W. C. Lim, H. J. Shin, J. P. Singh, S. O. Won and K. H. Chae, *Phys. Chem. Chem. Phys.*, 2017, **19**, 6397.

38 A. I. Frenke, *Chem. Soc. Rev.*, 2012, **41**, 8163.

39 Z. Sun, W. Yan, T. Yao, Q. Liu, Y. Xie and S. Wei, *Dalton Trans.*, 2013, **42**, 13779.

40 M. Newville, *Rev. Mineral. Geochem.*, 2014, **78**, 33.

41 M. Varshney, A. Sharma, H. J. Shin, H. H. Lee, T. Y. Jeon, B. H. Lee, K. H. Chae and S. O. Won, *J. Phys. Chem. Solids*, 2017, **110**, 187.

42 B. Choudhury and A. Choudhury, *Curr. Appl. Phys.*, 2013, **13**, 217.

43 J. G. Chen, *Surf. Sci. Rep.*, 1997, **30**, 1–152.

44 X. T. Zhou, F. Heigl, J. Y. P. Ko, M. W. Murphy, J. G. Zhou, T. Regier, R. I. R. Blyth and T. K. Sham, *Phys. Rev. B*, 2007, **75**, 125303.

45 F. Tourtin, P. Armand, A. Ibanez, G. Tourillon and E. Philippot, *Thin Solid Films*, 1998, **322**, 85.

46 M. Yamamoto, T. Yoshida, N. Yamamoto, T. Nomoto, Y. Yamamoto, S. Yagic and H. Yoshida, *J. Mater. Chem. A*, 2015, **3**, 16810.

47 S. Y. Chen, R. J. Chen, W. Lee, C. L. Dong and A. Gloter, *Phys. Chem. Chem. Phys.*, 2014, **16**, 3274.

48 K. Nishi, K. I. Shimizu, M. Tanamatsu, H. Yoshida, A. Satsuma, T. Tanaka, S. Yoshida and T. Hattori, *J. Phys. Chem. B*, 1998, **102**, 10190.

49 K. I. Shimizu, M. Tanamatsu, K. Nishi, H. Yoshida, A. Satsuma, T. Tanaka, S. Yoshida and T. Hattori, *J. Phys. Chem. B*, 1999, **103**, 1542.

50 D. Carta, M. F. Casula, G. Mountjoy and A. Corrias, *Phys. Chem. Chem. Phys.*, 2008, **10**, 3108.

51 V. Matolín, M. Cabala, I. Matolínová, M. Škoda, M. Václavů, K. C. Prince, T. Skála, T. Mori, H. Yoshikawa, Y. Yamashita, S. Ueda and K. Kobayashi, *Fuel Cells*, 2010, **10**, 139.

52 G. M. Criado, J. S. Ruiz, M. H. Chu, R. Tucoulou, I. López, E. Nogales, B. Mendez and J. Piqueras, *Nano Lett.*, 2014, **14**, 5479.

53 S. RajaAmbal, A. K. Yadav, S. N. Jha, D. Bhattacharyya and C. S. Gopinath, *Phys. Chem. Chem. Phys.*, 2014, **16**, 23654.

54 A. B. Getsoian, U. Das, J. C. Bunquin, G. Zhang, J. R. Gallagher, B. Hu, S. Cheah, J. A. Schaidle, D. A. Ruddy, J. E. Hensley, T. R. Krause, L. A. Curtiss, J. T. Miller and A. S. Hock, *Catal. Sci. Technol.*, 2016, **6**, 6339.

55 W. Gu, H. Wnag and K. Wang, *Dalton Trans.*, 2014, **43**, 6406.

56 J. Wong, Z. U. Rek, M. Rowen, T. Tanaka, F. Schifers, B. Mfiller, G. N. George, I. J. Pickering, G. Via, B. DeVries, G. E. Brown Jr and M. Frba, *Phys. B Condens. Matter*, 1995, **208–209**, 220.

57 B. Ravel and M. Newville, *J. Synchrotron Radiat.*, 2005, **12**, 537.

58 A. L. Ankudinov and J. J. Rehr, *Phys. Rev. B*, 1997, **56**, R1712.

59 J. F. Lee, M. T. Tang, W. C. Shin and R. S. Liu, *Mater. Res. Bull.*, 2002, **37**, 555.

60 T. Wang, S. S. Farvid, M. Abulikemu and P. V. Radovanovic, *J. Am. Chem. Soc.*, 2010, **132**, 9250.

61 T. Wang and P. V. Radovanovic, *J. Phys. Chem. C*, 2011, **115**, 18473.

62 M. Hegde, T. Wang, Z. L. Miskovic and P. V. Radovanovic, *Appl. Phys. Lett.*, 2012, **100**, 141903.

63 A. Sharma, M. Varshney, K. D. Verma, Y. Kumar and R. Kumar, *Nucl. Instrum. Methods Phys. Res., Sect. B*, 2013, **308**, 15.

64 A. Vij, S. Gautam, V. Kumar, R. Brajpuriya, R. Kumar, N. Singh and K. H. Chae, *Appl. Surf. Sci.*, 2013, **264**, 237.

65 H. Riesen and W. A. Kaczmarek, *Inorg. Chem.*, 2007, **46**, 7235.

66 L. Liu, Y. Wang, Y. Su, Z. Ma, Y. Xie, H. Zhao, C. Chen, Z. Zhang and E. Xie, *J. Am. Chem. Soc.*, 2011, **94**, 2141.